CHARACTERIZATION OF OPTICAL SURFACE PROPERTIES OF 1.3 GHz SRF CAVITIES FOR THE EUROPEAN XFEL*

M. Wenskat†, L. Steder, DESY, Hamburg, Germany

Abstract

The optical inspection of the inner surface of superconducting RF cavities is a well-established tool at many laboratories. Its purpose is to recognize and understand field limitations and to allow optical quality assurance during cavity production. Within the ILC-HiGrade program at DESY, as part of the XFEL cavity production, an automated image processing and analysis algorithm has been developed that recognizes structural boundaries. The properties of these boundaries can be used for characterization. The potential of this framework for automated quality assurance as an integral part of large-scale cavity production will be outlined.

OBACHT

A fully automated robot for optical inspection has been continuously used at DESY. It is equipped with a high-resolution camera, which resolves structures down to 12 µm for properly illuminated surfaces. The mechanical details of OBACHT, the optical system and the control are described in [1–3]. Figure 1 shows an image of the inner cavity surface taken with OBACHT.

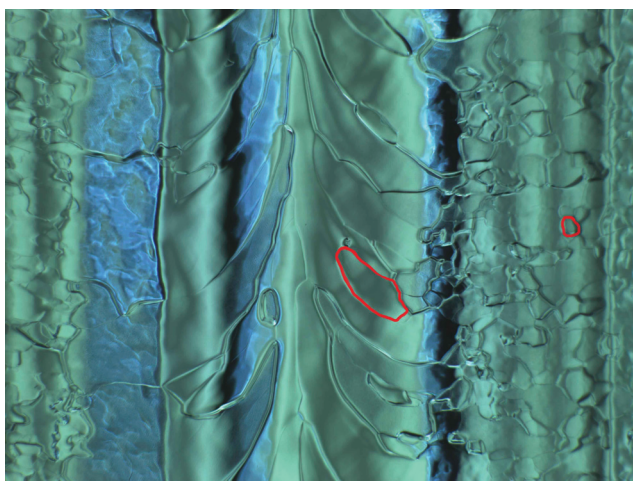

Figure 1: Image of the inner cavity surface with the equatorial welding seam in the image center taken with OBACHT. The image size is 9×12 mm^2. The red contours are examples of grain boundaries identified with the image processing algorithm.

* Work is funded from the EU 7th Framework Program (FP7/2007-2013) under grant agreement number 283745 (CRISP) and "Construction of New Infrastructures - Preparatory Phase", ILC-HiGrade, contract number 206711, BMBF project 05H12GU9, and Alexander von Humboldt Foundation.

† marc.wenskat@desy.de

The objects of interest within an image of the inner cavity surface are grain boundaries. In order to identify and quantify those boundaries, an image processing and analysis algorithm has been developed.

IMAGE PROCESSING AND ANALYSIS

The main goal of the image processing algorithm is to identify grain boundaries, regardless of their position within the image which is exposed to varying illumination, as can be seen in Figure 1. The approach of this algorithm is, by applying a sequence of high-pass filter and local contrast enhancements, to project pixels which belong to grain boundaries onto a uniform gray scale range, which is distinct to the background. After this projection, a histogram based segmentation of the image is performed. This segmentation assumes, that the image contains two classes of pixels (grain boundary and background), where the intensity values follow a bi-modal distribution, and calculates the optimum threshold separating the two classes. The output is a binary image with the same size as the input image. It will contain grain boundary pixels in white (logical one) and background pixels in black (logical zero). As a last step, group of connected white pixels which form a grain boundary have to be classified as a single object and a labeled binary image is obtained. For more details on the image processing algorithm see [3]. An example of such a binary image is given in Figure 2.

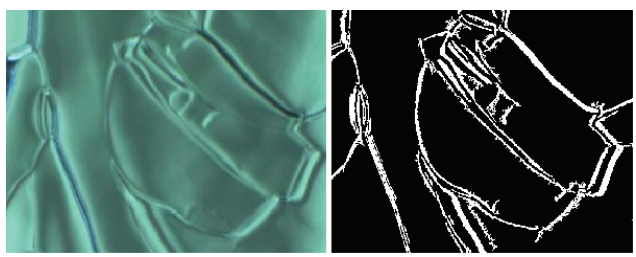

Figure 2: Left: a detail of an OBACHT image is shown. Right: the same detail after the image processing algorithm is shown. Features like grain boundaries (white) are visible.

Features can be identified in the binary image. Those are grain boundaries with varying width, so that an area can be ascribed, as well as an eccentricity, a centroid and an orientation. The grain boundary area is the total amount of pixels, of which a boundary consist of. This number is retrieved from the binary image and then multiplied by the *pixel size*, which is a property of the optical system. At OBACHT, this value is 12.25 µm^2. Other variables, such as a measure for the surface roughness based on the intensity gradient, include information from the original image.

ISBN 978-3-95450-178-6

SURFACE CHARACTERIZATION

At the time of the analysis, 14 cavities from RI were inspected, where each cavity underwent as final surface treatment an electro polishing (EP) and 31 cavities from Ettore Zanon, which received a buffered chemical polishing (BCP) as final surface treatment. The observed grain boundary area distribution per equator can be seen in Figure 3.

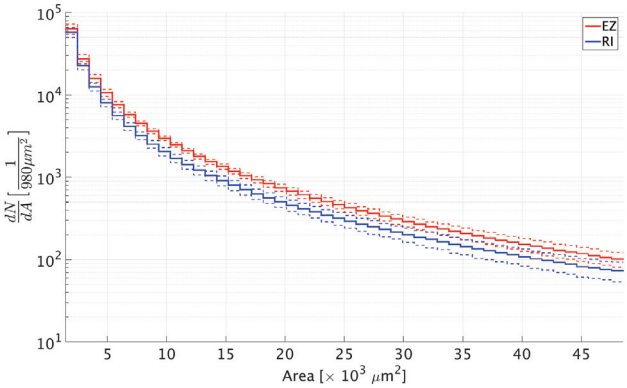

Figure 3: Average grain boundary area distribution of an equator. The blue distribution shows the average of 126 RI equators, the red distribution shows the average of 279 Ettore Zanon equators. The dotted lines are the 1σ confidence intervals of the average.

It can be seen that Research Instruments cavities exhibit a smaller number of boundaries with an area above $5 \cdot 10^3$ µm^2 than Ettore Zanon cavities. Motivated by the assumption that grain boundaries contribute to performance limitation mechanisms, a property called *integrated grain boundary area* is defined. It is the total grain boundary area measured in the equator region of a cell.

The cell with the largest integrated grain boundary area per cavity is called the *optically conspicuous cell*. Figure 4 shows the histogram of the observed values of the integrated grain boundary area of the optically conspicuous cells fo 31 cavities from Ettore Zanon. The integrated grain boundary area averages at about 1600 mm^2, hence covering about 20% of the weld area. For Research Instruments, the average is about 1200 mm^2 and the coverage rate is 15%. The distribution of the optically conspicuous cells within the cavity is shown in Figure 5. For Ettore Zanon, equator 9 is the conspicuous cell in 24 out of 31 cases. For Research Instruments, equators 6 and 7 are the conspicuous cells in 9 out of 14 cases. The χ^2-test for both vendors showed a statistical significant deviation of the observed distribution from a uniform distribution with a χ^2 of 17 for Research Instruments and a χ^2 of 112 for Ettore Zanon and the degrees of freedom (df) of 8 for both.

The cell with the smallest integrated grain boundary area of a individual cavity is called the *optically best cell*. The distribution of the optically best cells within the cavity is shown in Figure 6. For Ettore Zanon, the χ^2-test showed

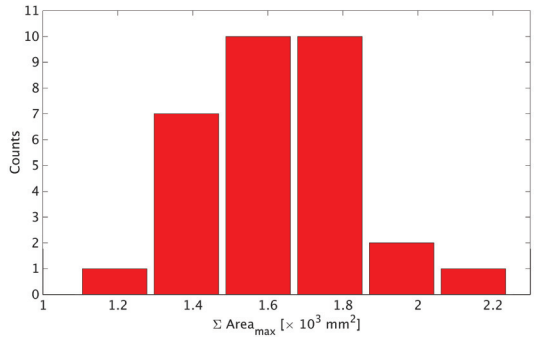

Figure 4: Histogram of the values of the integrated grain boundary area for the 31 optically conspicuous cells from Ettore Zanon.

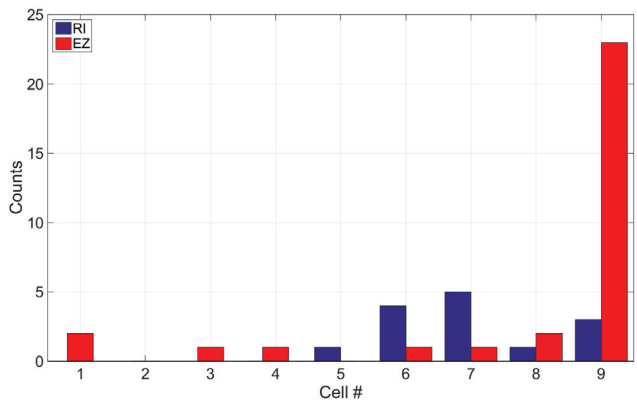

Figure 5: Observed longitudinal distribution of the *optically conspicuous cells*. The blue distribution is derived from 14 Research Instruments (RI) cavities, the red distribution from 31 Ettore Zanon (EZ) cavities.

that the observed distribution is in agreement with a uniform distribution with a χ^2 of 8.2 and the df 8. For Research Instruments, equators 1 and 4 are favoured. The χ^2-test for a uniform distribution yields χ^2 of 32 and the df 8. It is interesting to note, that the observed cells, which are most likely to be the optically conspicuous or best cell, are cells with a special position in the vendor specific welding sequence. For Ettore Zanon, the equatorial weld 9 is the first to be welded and the other welds follow in a alternating sequence. At Research Instruments, the first step is the fabrication of assembly groups in which the assembly and equatorial welds of two 3.5 cell cavities [E1-3] and [E7-9] and one double dumbbell [E5] are done. In a final assembly and welding step of those assembly groups, equators 4 and 6 are welded.

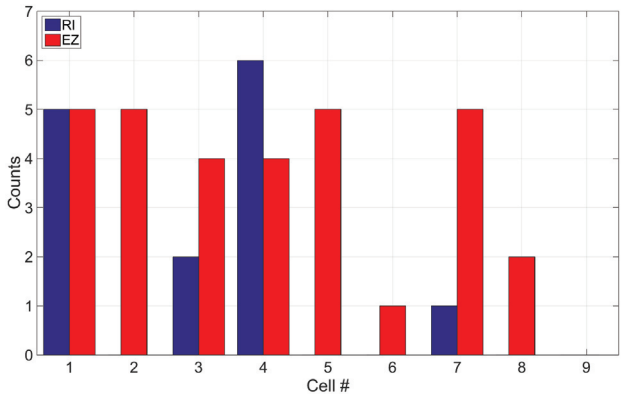

Figure 6: Observed longitudinal distribution of the *optically best cells*. The blue distribution is derived from 14 Research Instruments (RI) cavities, the red distribution from 31 Ettore Zanon (EZ) cavities.

EQUATORIAL WELD OF OPTICAL CONSPICUOUS CELLS

The integrated boundary area of three cells exceed the average value by more than 25% and one cell is below the average value by 25%, see Figure 4. For a better understanding on the origin of this deviation, the integrated grain boundary area per image against the angular position of the image taken for these cells is shown in Figure 7.

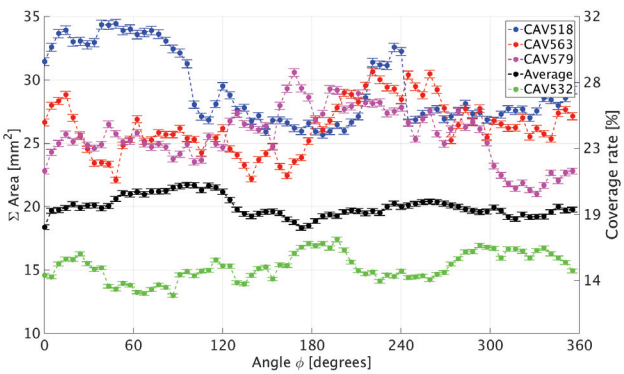

Figure 7: Integrated grain boundary area per image against the angular position of the image taken for the three cells with the largest values, the average of the whole set and the cell with the smallest value.

Images of the specific cells significantly exceeding the average are shown in Figures 8 and 9. In comparison to this excess, Figure 10 shows an image of the inner cavity surface with a smaller than average integrated grain boundary area per image.

CAV518, Figure 8, shows some remnants of the machining procedure prior to welding. In addition, the cavity required an equator weld repair. Although all equators of CAV00518

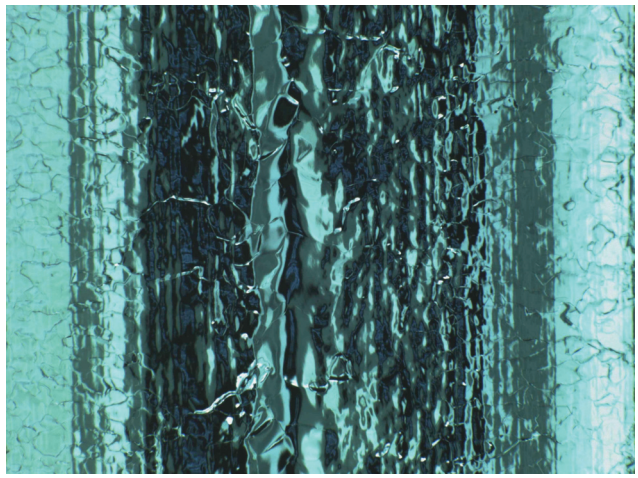

Figure 8: OBACHT image of the inner cavity surface of cavity CAV518, equator 9, 225.6 degree.

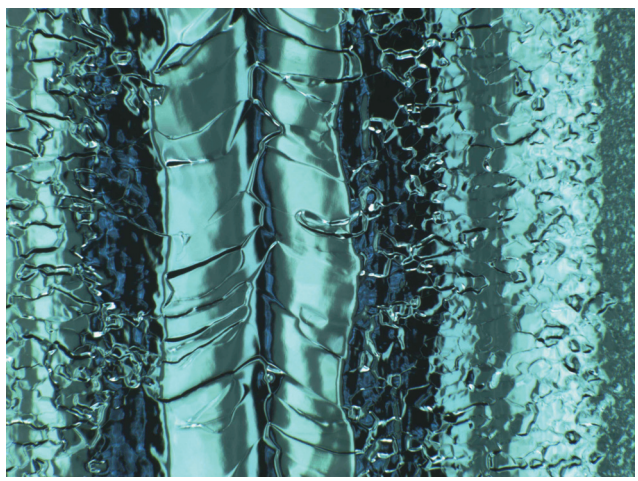

Figure 9: OBACHT image of the inner cavity surface of cavity CAV563, equator 9, 249.6 degree.

showed a larger integrated grain boundary area than average, equator nine was outstanding.

CAV563, Figure 9, shows prominent grain boundaries in the welding seam and heat affected zone. This topography was observed in several cavities, although mostly in equator nine and in different intensities. A process which could cause such a pattern has not been identified yet. The inspection of the cell surface next to the equatorial weld showed no comparable topography. Hence one suspects welding procedure.

CAV532, Figure 10, is a cavity with an overall homogenous and smooth appearance.

In order to estimate the influence of the surface chemistry on the observed values of the integrated grain boundary area, images of the bulk niobium were analysed. Those so called *cell images* are taken with an offset of ±11.5 mm relative to the equator images routinely during the inspections.

ISBN 978-3-95450-178-6

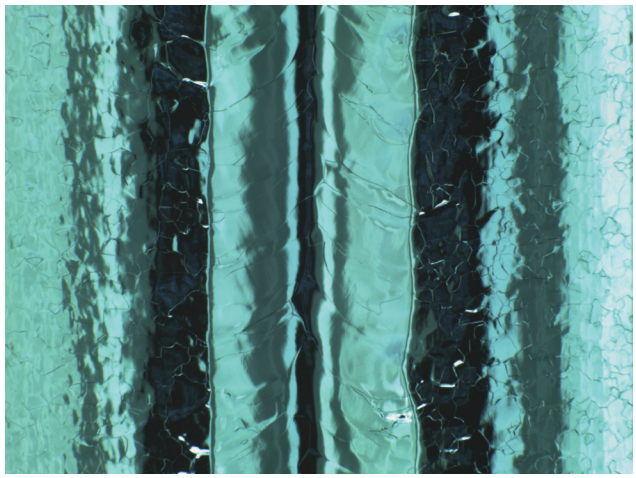

Figure 10: OBACHT image of the inner cavity surface of cavity CAV532, equator 6, 182.4 degree.

Hence, only an influence of the surface chemistry and not from the assembly or electron beam welding in these images is expected. The average value of the integrated area distributions in the cell images for Research Instruments is 28 ± 4 mm^2 per image and for Ettore Zanon 25 ± 3 mm^2 per image. In contrast to the equator images, where a factor of two between the smallest and largest value within a single vendor was observed, the niobium surface in the bulk is comparable within uncertainties for all inspected cavities. This leads to the conclusion that the assembly and electron beam welding procedure is the most significant influence on the integrated grain boundary area, and the optical effect of the surface chemistry in the equator images can be neglected. In a next step, a possible influence of these procedures onto the RF performance is studied. Although only cavities from Ettore Zanon are discussed in detail in this work, cavities from Research Instruments, were included in a more detailed analysis [3]. Table 1 shows a comparison of the achieved accelerating field of a cavity against the average integrated grain boundary area per image of the optically conspicuous cell of this cavity.
The results suggest that higher $E_{\mathrm{acc,max}}$ can be reached when the integrated grain boundary area is small.

Table 1: Comparison of the RF results and the integrated grain boundary area per image.

Cavity	$E_{\mathrm{acc,max}}$ [MV/m]	$< \Sigma A >_{\mathrm{im}}$ [mm^2]
CAV518	22	28
CAV563	20	26
CAV579	25	24
<EZ>	28 ± 7	20 ± 2
CAV532	35	15

SUMMARY

Within the scope of the European XFEL cavity production and the ILC-HiGrade research program, an automated image analysis algorithm has been developed. Such an algorithm is useful for a quality assurance of a large-scale cavity production, which is foreseen for the ILC. With this algorithm, a characterization of the inner cavity surface in terms of optical properties was done. This characterization is based on a global quantification of the surface rather than local defects. The surface characterization leads to an observation of vendor specific distributions of important surface properties like the grain boundary area. Statistical analysis of those distributions suggest that the assembly and electron beam welding procedure is critical for obtaining high electric fields.

ACKNOWLEDGMENT

I would like to thank J. Iversen, D. Reschke, W. Singer (MHF-sl) and A. Matheisen (MKS3) for their support, insights and many valuable discussions. Furthermore, I would like to thank S. Aderhold (Fermilab), A. Navitski, J. Schaffran and Y. Tamashevich (FLA-ILC) for their work. Otherwise, mine would have been impossible.

REFERENCES

[1] L. Steder, "Measurement Manual for OBACHT", ILC-HiGrade-Report-2012-001 (2012).

[2] M. Lemke et al., "OBACHT - Optical Bench for Automated Cavity Inspection with High Resolution on Short Time Scales", ILC-HiGrade-Report-2013-001 (2013).

[3] M. Wenskat, "Automated Surface Classification of SRF Cavities for the Investigation of the Influence of Surface Properties onto the Operational Performance", PhD thesis, University of Hamburg (2015).